




Cite this: *RSC Adv.*, 2025, 15, 13442

# A Spin-polarized DFT study of functionalized MXenes as effective anchor materials in lithium-sulfur batteries†

Yize Niu, Ying Jiang, Feihu Zou, Weiqi Song, Yue Zhao, Hongye Zhang, Qiang Li \* and Yuanyuan Pan \*

Lithium-sulfur (Li-S) batteries have attracted great enthusiasm in recent years due to ultra-high theoretical energy densities, abundant sulfur electrode resources and low price. Despite the severe shuttle effect of lithium polysulfides (LiPSs), the poor conductivity of  $S_8$  and its intermediate products, and the relatively slow dynamics, pose significant challenges for the commercial application of Li-S batteries. Here, functionalized MXenes  $M_2CT_2$  ( $M = V, Cr, Mn, \text{ and } Mo$ ;  $T = F \text{ and } O$ ) used as the sulfur host are studied to build multifunctional cathodes *via* spin-polarized first-principles calculation. Through analyzing the adsorption energy and configuration of  $S_8/Li_2S_n$  adsorbed  $M_2CT_2$ , it is found that spin polarization is indispensable to the Li-S battery calculation of MXenes with transition metals. With the spin polarization calculation, the  $M_2CT_2$  exhibit moderate anchoring strengths and stable adsorption structures, which effectively mitigates the polysulfide shuttle phenomenon. The low decomposition barriers of  $Li_2S$  (0.27–1.00 eV) and low diffusion barriers of  $Li^+$  (0.11–0.44 eV) of  $M_2CT_2$  are observed, which effectively improve the rate performance of batteries. Among the studied MXenes,  $V_2CO_2$  and  $Mo_2CO_2$  are the best choices of host materials for LiPSs with metallic characteristics, outstanding electrocatalysis performance, low decomposition barriers of  $Li_2S$ , and diffusion barriers of  $Li^+$ . This work provides important insights into spin-polarized electrode materials for enhanced energy storage capabilities by investigating the application of intrinsic magnetic MXene compounds.

Received 26th February 2025

Accepted 20th April 2025

DOI: 10.1039/d5ra01387a

rsc.li/rsc-advances

## Introduction

With the continuous growth of energy demand, it is an urgent task to develop high-performance and affordable rechargeable batteries. Lithium-sulfur (Li-S) batteries have attracted substantial research interest in recent years, owing to their high theoretical capacity and specific energy.<sup>1–4</sup> Based on the two-electron transfer redox reaction involving multiple steps, the theoretical capacity of Li-S batteries can reach up to 1675 mA h g<sup>−1</sup>. Moreover, sulfur is abundant on earth and inexpensive.<sup>5,6</sup> As a result, the combination of high theoretical capacity and low cost endows Li-S batteries with great application potential in the field of commercial batteries.<sup>7</sup> However, there is still a long journey ahead for Li-S batteries to achieve commercial application, which is hindered by several thorny issues. For example, the electrical conductivities of  $S_8$  and  $Li_2S_n$  are poor, and the reaction kinetics is sluggish due to the high decomposition energy barrier of  $Li_2S$ .<sup>8,9</sup> During the cycling process, intermediate products of lithium polysulfides (LiPSs)

are constantly generated. These intermediates can dissolve in the electrolyte, resulting in a reduction of active sulfur species. In particular, long-chain LiPSs ( $Li_2S_n$ ,  $n = 4, 6, \text{ and } 8$ ) will migrate to the lithium metal anode and deposit there by shuttling through the separator, which also results in a rapid decline in the battery's capacity.<sup>10,11</sup> In the future, more efforts should be devoted to suppressing the shuttle effect. An ideal sulfur composite cathode is capable of suppressing the shuttle effect by moderately anchoring  $Li_2S_n$ , enhancing the sulfur reduction reaction (SRR), and improving the reaction kinetics.<sup>12–14</sup>

MXenes, a novel class of two-dimensional transition metal carbides and nitrides, exhibit remarkable capabilities in electrochemical energy storage systems. These materials combine metallic-grade conductivity with ultrafast charge migration kinetics and exceptional surface charge storage capacity, attributes that have positioned them at the forefront of energy research since their 2011 discovery.<sup>15</sup> Following Gogotsi's pioneering synthesis of  $Ti_3C_2$  in 2011, titanium-based MXenes have dominated Li-S battery research due to their exceptional interfacial compatibility and sulfur confinement capabilities.<sup>16</sup> After the first synthesis of  $Ti_3C_2$ ,  $M_3C_2$  has been extensively studied and is considered to be a cathode material for Li-S batteries with excellent performance. Recent experimental studies proved that  $M_2C$  is thinner than  $M_3C_2$ , which has also proven to be a good

College of Physics, Center for Marine Observation and Communications, Qingdao University, Qingdao, China. E-mail: liqiang@qdu.edu.cn; panyy@qdu.edu.cn

† Electronic supplementary information (ESI) available. See DOI: <https://doi.org/10.1039/d5ra01387a>



anchoring material for Li-S batteries with high specific capacity and long cycle life.<sup>17,18</sup> MXenes synthesized *via* HF etching typically exhibit surface terminations dominated by oxygen (O) and fluorine (F) groups, which could enhance material stability, optimize interface interaction and improve electrochemical performance.<sup>19,20</sup> According to previous reports,  $\text{Ti}_2\text{C}(\text{OH})_2$  and  $\text{V}_2\text{C}(\text{OH})_2$  exhibit excessively strong interfacial interactions with LiPSs, inducing premature decomposition of active species.<sup>21,22</sup> Conversely, oxygen-terminated MXenes like  $\text{Ti}_2\text{CO}_2$  and  $\text{Ti}_2\text{NO}_2$  demonstrate optimal chemisorption energetics for LiPSs anchoring.  $\text{Ti}_2\text{CF}_2$  and  $\text{Ti}_2\text{NF}_2$  achieve balanced binding interactions, with systematic analyses revealing that O- and F-terminated MXenes collectively offer superior polysulfide confinement capabilities compared to OH-terminated MXenes.<sup>23,24</sup> The interaction between the polysulfides and the hydroxide-terminated or no functionalized MXene is very strong, which could distort the polysulfides and the MXene materials. Therefore, they cannot effectively suppress the shuttle effect.<sup>25–27</sup> Recently,  $\text{V}_2\text{NO}_2$  and  $\text{V}_2\text{NF}_2$  MXenes have been widely investigated due to low decomposition barriers of  $\text{Li}_2\text{S}$  and diffusion barriers of  $\text{Li}^+$ , which could accelerate reaction kinetics during the discharge and charging process. The structural diversity of MXenes motivates systematic exploration of their electrochemical properties, particularly focusing on surface-engineered variants with functional groups. It is an interesting task to explore other MXene materials that possess outstanding electrochemical performance, particularly those MXene materials with a large number of functional groups and those that have undergone surface modification.<sup>28,29</sup>

In our work, a series of  $\text{M}_2\text{CT}_2$  ( $\text{M} = \text{V}, \text{Cr}, \text{Mn}, \text{and Mo}$ ;  $\text{T} = \text{F}$  and  $\text{O}$ ) are selected as sulfur hosts to construct multifunctional cathode material *via* spin-polarized first-principles calculations. We note the adsorption energy of  $\text{S}_8/\text{Li}_2\text{S}_n$  adsorbed  $\text{M}_2\text{CT}_2$  is greatly reduced from non-spin-polarized system to spin-polarized system. Spin-polarized systems provide a critical framework for comprehensively elucidating interfacial phenomena in transition metal composites at atomic scales. The adsorption energy of  $\text{S}_8/\text{Li}_2\text{S}_n$  adsorbed  $\text{M}_2\text{CT}_2$  range from 0.63 eV to 5.15 eV, which indicates the  $\text{M}_2\text{CT}_2$  could inhibit the shuttle effect and reduce the loss of active sulfur species in the polarization system. We find that  $\text{S}_8$  can be efficiently reduced to  $\text{Li}_2\text{S}$  with a small rare-limiting step (0.51–1.37 eV), indicating the superior sulfur reducing ability of  $\text{M}_2\text{CT}_2$ . Moreover, the decomposition barriers of  $\text{Li}_2\text{S}$  and migration barriers of  $\text{Li}^+$  for  $\text{M}_2\text{CO}_2$  are lower than those for  $\text{M}_2\text{CF}_2$  during charging process, which ultimately promotes redox kinetics during cycling. Based on the finding presented above, we identified  $\text{V}_2\text{CO}_2$  and  $\text{Mo}_2\text{CO}_2$  as promising candidates for host materials with moderate anchoring strength and excellent electrocatalytic performance. Systematic analysis of MXene functionalities in this work provides actionable strategies for tailoring their interfacial properties toward sulfur cathode optimization.

## Computational details

Spin-polarized density functional theory (DFT) calculations are carried out using the Vienna *Ab Initio* Simulation Package

(VASP), employing the Perdew–Burke–Ernzerhof (PBE) generalized gradient approximation (GGA) functional to describe exchange-correlation effects.<sup>30,31</sup> The core-electron interactions are treated through the projector-augmented wave (PAW) methodology, with a plane-wave basis set truncated at 500 eV kinetic energy. For Brillouin zone integration in the  $4 \times 4$  supercell's two-dimensional geometry, a Monkhorst–Pack grid of  $5 \times 5 \times 1$   $k$ -points is implemented.<sup>32</sup> To better characterize the strongly correlated 3d electron systems, we incorporate the Hubbard U correction within the GGA + U framework.<sup>33</sup> According to the previous works, the U values of V, Cr, Mn, and Mo atoms are set to be 3, 4, 3, and 3 eV, respectively.<sup>22,34–36</sup> Long-range van der Waals interactions are accounted for using the DFT-D3 empirical dispersion correction scheme.<sup>37</sup> A minimum vacuum spacing of 20 Å perpendicular to the surface plane is maintained to eliminate artificial periodic interactions. Structural optimizations are performed until achieving convergence thresholds of  $1.0 \times 10^{-5}$  eV per atom for total energy and  $0.01 \text{ eV } \text{\AA}^{-1}$  for residual forces. The migration mechanisms of  $\text{Li}^+$  on  $\text{M}_2\text{CT}_2$  surfaces are investigated through the climbing image nudged elastic band (CI-NEB) method, which enables precise determination of minimum energy pathways and activation barriers.<sup>38</sup> The thermodynamic stability of  $\text{Li}_2\text{S}$  adsorption on  $\text{V}_2\text{CO}_2$  and  $\text{Mo}_2\text{CO}_2$  is simulated by *ab initio* molecular dynamics (AIMD) at 300 K. The NVT ensemble simulations are conducted for 5 ps with a time step of 1.0 fs, corresponding to 5000 simulation steps. Detailed calculation equation of adsorption energies ( $E_{\text{ads}}$ ), charge density difference (CDD), and the equations of Gibbs free energy change ( $\Delta G$ ) are comprehensively derived in the ESI† section.

## Results and discussions

### Configuration, magnetic ground state and electronic conductivity of $\text{M}_2\text{CT}_2$

Investigating MXenes with different magnetic transition metal constituents offers a strategic pathway to leverage their compositional versatility for improving sulfur electrochemistry in Li-S systems. Therefore, the  $\text{M}_2\text{C}(\text{F/O})_2$  with the transition metals ( $\text{M} = \text{V}, \text{Cr}, \text{Mn}, \text{and Mo}$ ) are chosen as sulfur hosts in our work. The monolayer  $\text{M}_2\text{C}$  MXene adopts a  $P3m1$ -symmetric honeycomb lattice, featuring a stratified architecture where hexagonally arranged carbon atoms are intercalated between two metallic M layers, as structurally resolved in Fig. 1a.<sup>39</sup> There are five possible configurations for terminal groups ( $\text{T} = \text{F}$  and  $\text{O}$ ) absorbed on the M atom in Fig. S1†: (a) T atoms locate right above the M atoms (Top sites); (b) T atoms locate at the hollow sites of adjacent C atoms (Hcp sites); (c) T atoms locate at the hollow sites of contralateral M atoms (Fcc sites); (d) T atoms located at the Fcc and Hcp sites (Fcc–Hcp); (e) T atoms located at the Hcp and Top sites (Fcc–Hcp). The stable configurations of  $\text{M}_2\text{CT}_2$  are Fcc structures, except for  $\text{Cr}_2\text{CO}_2$  and  $\text{Mo}_2\text{CO}_2$ , which are Hcp structures as shown in Fig. 1c. The basic information of their lattice parameters is listed in Table S1.†

Considering that magnetic transition metal in the  $\text{M}_2\text{CT}_2$ , five types of magnetic ground state structures are calculated in Fig. 2: non-magnetic (NM), ferromagnetic (FM), and

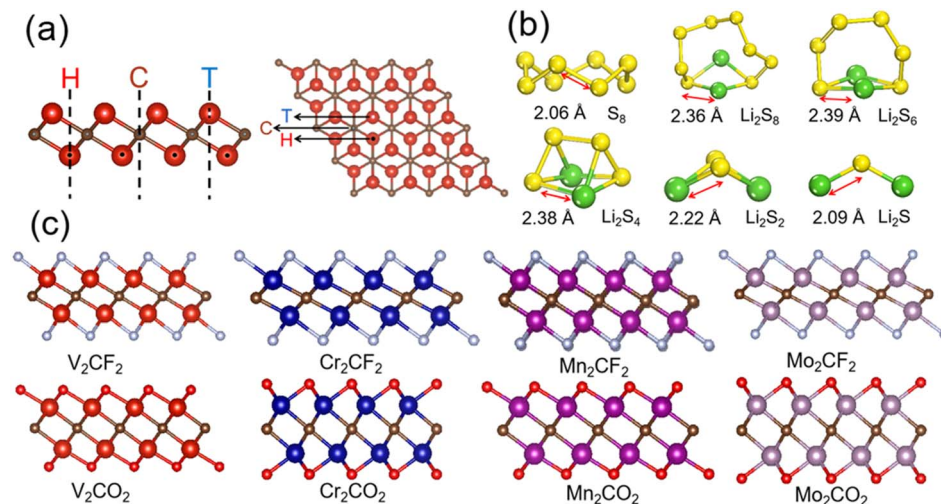


**Fig. 1** (a) Top and side views of MXene monolayer with different adsorption sites (hollow site (H), carbon-top site (C) and transition metal-top (T)). (b) Geometrical structures of  $S_8$  and  $Li_2S_n$  molecules. (c) Side view of the stable atomic structures of  $V_2CT_2$ ,  $Cr_2CT_2$ ,  $Mn_2CT_2$ , and  $Mo_2CT_2$  with the terminal groups  $T = O$  and  $F$ . Yellow, green, dark red, brown, light red, white, blue, dark purple and light purple color balls represent the S, Li, V, C, O, F, Cr, Mn and Mo atoms, respectively.

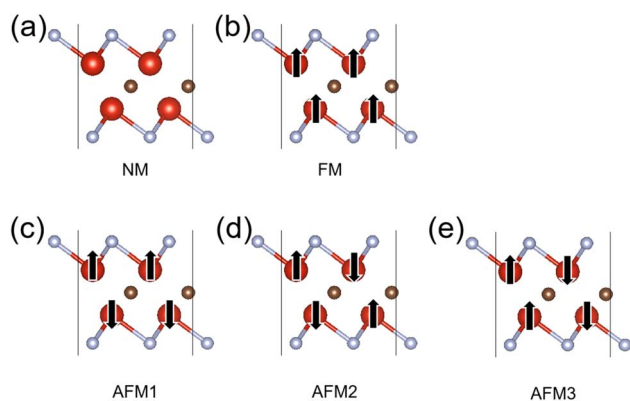


**Fig. 2** Magnetic state configurations of  $M_2CT_2$ : (a–e) NM, FM, AFM1, AFM2, AFM3, respectively (taking a  $2 \times 2$   $V_2CF_2$  supercells as an example). The directions of the arrow represent the spin up and down.

antiferromagnetic (AFM1, 2, and 3). After relaxation, it is found that stable structures of  $V_2CO_2$  and  $Mo_2CO_2$  are NM, while the stable structures of other  $M_2CT_2$  are AFM, except that  $Mn_2CF_2$  and  $Cr_2CO_2$  are FM structures. The calculated magnetic ground states are same as the results of the previous studies.<sup>34,40–42</sup> According to the crystal field theory, the magnetic exchange interactions in the 2D magnetic materials mainly originate from two kinds of mechanisms:<sup>43–45</sup> (i) the super-exchange ferromagnetism between the nearest intra-layered M atoms *via* the outmost oxygen atom (*e.g.*, Cr–O–Cr and Mn–F–Mn). (ii) The antiferromagnetic interactions between the nearest interlayered M atoms *via* the carbon atom (*e.g.* Cr–C–Cr and Mn–C–Mn). In this case, the ferromagnetic super-exchange processes start to compete with the antiferromagnetic super-exchange mechanism.

Meanwhile, the limited conductivity of sulfur represents another key challenge impeding the advancement of Li-S

batteries. To further study the electronic structural properties of  $M_2CT_2$ , we calculate the projected density of states (PDOS) of  $M_2CT_2$ . As shown in Fig. 3,  $V_2CO_2$  and  $Mo_2CO_2$  show significant metallic conductivity, while the others are semiconductors, except for  $Mn_2CF_2$ , which is a special semimetal. The DOS of the  $M_2CT_2$  mainly comes from the d-orbital of the transition metal. Furthermore, it is found that the  $d_{xy}$  and  $d_{x^2-y^2}$  orbitals are degenerated, while the  $d_{xz}$  and  $d_{yz}$  orbitals are degenerated at their respective energy levels as presented in Fig. S2.†

### Anchoring of $M_2CT_2$ to inhibit shuttle effect

During Li-S battery discharge, LiPSs dissolve into the electrolyte and shuttle toward the anode through the separator, leading to progressive depletion of electroactive sulfur species. Optimal cathode materials require appropriate adsorption energies to immobilize LiPSs and prevent active sulfur depletion.<sup>46,47</sup> Before to study the anchor ability of  $M_2CT_2$  for  $S_8$  and  $Li_2S_n$ , the  $S_8$  and  $Li_2S_n$  are optimized in  $10 \times 10 \times 10 \text{ \AA}^3$  cell, and the relaxed structures are shown in Fig. 1b. The S–S bond length in  $S_8$  is determined to be 2.06 Å. The Li–S bond lengths in  $Li_2S_8$ ,  $Li_2S_6$ ,  $Li_2S_4$ ,  $Li_2S_2$  and  $Li_2S$  are determined to be 2.36 Å, 2.39 Å, 2.38 Å, 2.22 Å and 2.09 Å, respectively. These structures of our work are consistent with the previous reports.<sup>40,48,49</sup>

To evaluate the anchor performance of the functionalized  $M_2CT_2$ , we calculated the adsorption energy ( $E_{\text{ads}}$ ) of  $S_8$  and  $Li_2S_n$  on these  $M_2CT_2$  surface as a key parameter, which is defined in the ESI.† The positive values of the adsorption energies indicate that adsorption could proceed spontaneously, and moderate adsorption energy represents good anchoring ability. The  $E_{\text{ads}}$  with spin-polarized and non-spin-polarized calculations are listed in Table 1 and Table S2,† respectively. The calculated  $E_{\text{ads}}$  for  $S_8$  and  $Li_2S_n$  on  $V_2CT_2$  and  $Cr_2CT_2$  are well consistent with those from the previous report.<sup>50</sup> For the adsorption of the  $S_8$  and  $Li_2S_n$ , a similar binding trend is





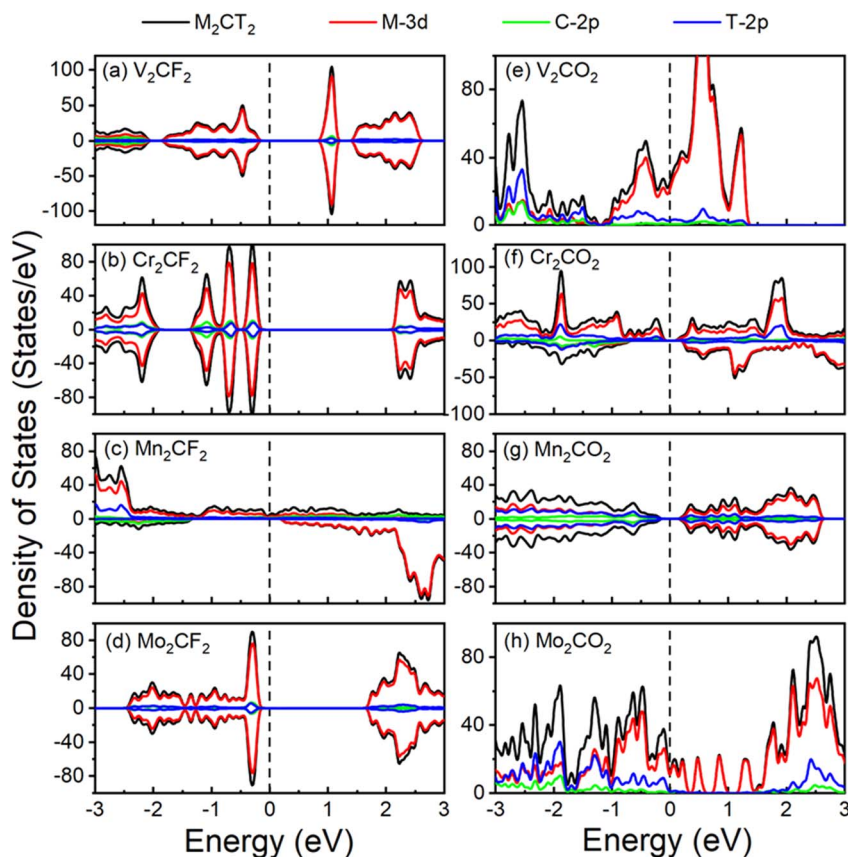


Fig. 3 Projected density of states of (a)  $V_2CF_2$ , (b)  $Cr_2CF_2$ , (c)  $Mn_2CF_2$ , (d)  $Mo_2CF_2$ , (e)  $V_2CO_2$ , (f)  $Cr_2CO_2$ , (g)  $Mn_2CO_2$ , and (h)  $Mo_2CO_2$ . The Fermi level is set at zero.

Table 1 The absorption energies  $E_{ads}$  (eV) of the  $S_8$  and LiPSs on  $M_2CT_2$  and  $M_2CO_2$  with the spin-polarized calculations

MXene	$S_8$	$Li_2S_8$	$Li_2S_6$	$Li_2S_4$	$Li_2S_2$	$Li_2S$
$V_2CF_2$	0.80	1.14	1.05	1.47	2.08	2.27
$Cr_2CF_2$	0.76	1.01	0.97	0.91	1.24	1.41
$Mn_2CF_2$	0.63	1.17	1.16	1.99	2.35	2.58
$Mo_2CF_2$	0.88	1.19	1.12	1.10	1.72	2.50
$V_2CO_2$	1.02	2.07	2.02	3.30	3.48	4.37
$Cr_2CO_2$	1.04	2.40	2.12	3.64	4.10	3.73
$Mn_2CO_2$	0.89	2.37	2.30	3.70	4.27	4.01
$Mo_2CO_2$	1.38	3.44	3.13	4.38	4.24	5.15

observed in all the calculated  $M_2CT_2$  as shown in Fig. 4. For all the calculated  $M_2CT_2$ , the  $E_{ads}$  values of the  $S_8$  are comparable. In addition, we note that the  $E_{ads}$  values increase with a decrease in the size of LiPSs.

It is also found that the  $E_{ads}$  of  $S_8$  and  $Li_2S_n$  on  $M_2CT_2$  surface with the spin-polarized calculations are significantly reduced compared with those of the non-spin-polarized calculations. The  $E_{ads}$  of  $Li_2S_n$  on  $V_2CF_2$  and  $Mn_2CF_2$  are reduced by 0.73–1.14 eV from the non-spin-polarized system to the spin-polarized system, while the  $E_{ads}$  values of  $Li_2S_n$  absorbed on  $Cr_2CO_2$  decreases by 0.62–2.44 eV. Meanwhile, the  $E_{ads}$  of  $Li_2S_n$  absorbed on  $Cr_2CF_2$  and  $Mo_2CF_2$  decreases by 2.10–3.55 eV,

which is nearly three times that of  $V_2CF_2$  and  $Mn_2CF_2$ .<sup>50–52</sup> The effect of the spin-polarization also reflected from the relaxed configuration of  $M_2CT_2-S_8/Li_2S_n$ . As presented in Fig. 5 and Fig. S3.† The atomic structure of  $Mn_2CO_2$  cannot even maintain at the NM state. The short-chain polysulfides break their bonds, and the substrate  $M_2CT_2$  undergo severe deformation under the spin-polarized calculation. The spin polarization system has a significant effect on the absorption process for the magnetic  $M_2CT_2$ . Therefore, we take the accurate spin-polarized calculation in the subsequent. The adsorption strength of the  $M_2CT_2$  for  $Li_2S_n$  follows the sequence:  $Mn_2CF_2 > V_2CF_2 > Mo_2CF_2 > Cr_2CF_2$  and  $Mo_2CO_2 > Mn_2CO_2 > Cr_2CO_2 > V_2CO_2$ , respectively. It clearly shows that the  $E_{ads}$  of  $S_8/Li_2S_n$  on  $M_2CT_2$  are much smaller than that on  $M_2C$ .<sup>52</sup> The enhanced covalent bonding characteristics between Li and S atoms in low-order LiPSs facilitate accelerated electron transfer from Li to S, creating vacant d-orbitals capable of accepting electrons from transition metal (T) atoms. Computational analyses reveal that short-chain LiPSs ( $Li_2S_2/Li_2S$ ) and  $Li_2S_4$  adopt specific geometric arrangements where dual lithium atoms remain proximal to the substrate surface, demonstrating strong chemisorption behavior. Conversely, long-chain species ( $Li_2S_8$  and  $Li_2S_6$ ) exhibit monodentate adsorption configurations with a single lithium atom near the interface, accompanied by horizontally oriented  $S_8$  molecular adsorption. Crucially, all adsorbed LiPSs

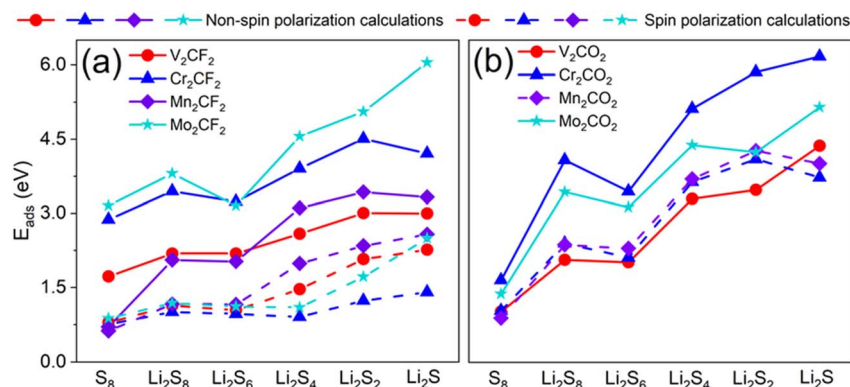


Fig. 4 The absorption energies of  $S_8/Li_2S_n$  adsorbed on (a)  $M_2CF_2$  and (b)  $M_2CO_2$  monolayer. The dotted and solid lines represent the absorption energy with the spin-polarized and the non-spin-polarized calculations, respectively.

configurations maintain structural integrity during electrochemical cycling, showing no signs of dissociation. It ensures reliable polysulfide retention on  $M_2CT_2$  surfaces throughout charge/discharge processes.

To effectively suppress polysulfide shuttling, the adsorption energetics of high-order  $Li_2S_n$  ( $n = 4, 6$ , and  $8$ ) on the sulfur host

matrix should surpass those with conventional ether-based electrolytes 1,3-dioxolane/1,2-dimethoxyethane (DOL/DME), thereby preventing electrolyte-mediated active material dissolution and capacity fade.<sup>53</sup> Given the preferential solubility of high-sulfur-content LiPSs in organic electrolytes, we systematically evaluated the adsorption energetics of long-chain LiPSs

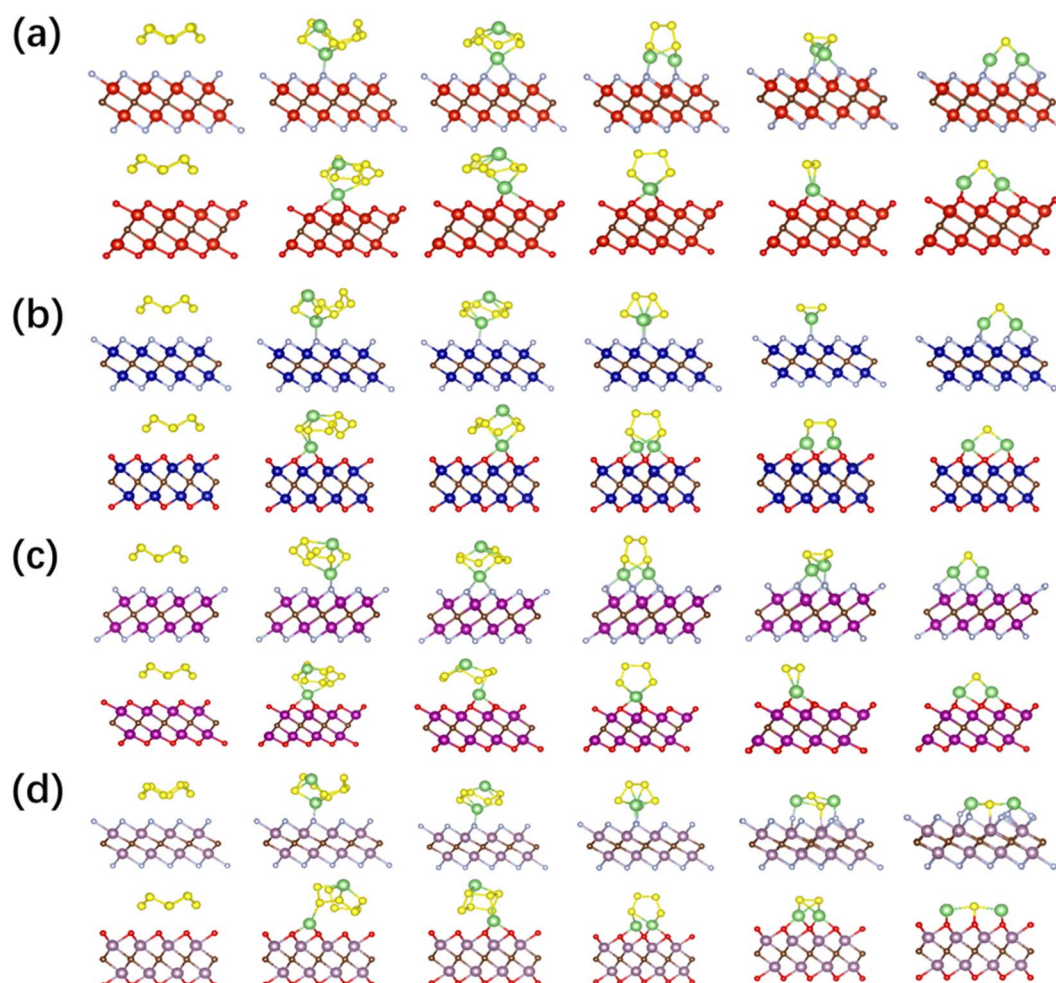


Fig. 5 The optimized structures of  $S_8/Li_2S_n$  adsorption on (a)  $V_2CT_2$ , (b)  $Cr_2CT_2$ , (c)  $Mn_2CT_2$ , and (d)  $Mo_2CT_2$  monolayer with the spin-polarized calculations.



( $\text{Li}_2\text{S}_8$ ,  $\text{Li}_2\text{S}_6$ , and  $\text{Li}_2\text{S}_4$ ) on DOL and DME. Structural optimizations of both isolated electrolyte molecules and LiPS-anchored complexes are shown in Fig. S4,<sup>†</sup> which reveal comparable polysulfide-trapping capabilities between DOL and DME, with adsorption energies spanning 0.75–0.90 eV. These values are significantly lower than those observed for  $\text{M}_2\text{CO}_2$  substrates and marginally reduced compared to  $\text{M}_2\text{CF}_2$  interfaces, highlighting the limited chemical confinement capacity of organic electrolytes relative to engineered MXene surfaces. Based on the aforementioned analysis,  $\text{M}_2\text{CT}_2$  is capable of anchoring  $\text{S}_8/\text{Li}_2\text{S}_n$  with a suitable  $E_{\text{ads}}$  value, while, it can preserve the integrity of the adsorption structures. In a tug-of-war with solvent molecules,  $\text{M}_2\text{CO}_2$  shows stronger chemical affinity for the LiPSs, which reveals its potential to serve as a type of host material for sulfur cathodes.

In order to explore the essence of the adsorption behavior between  $\text{S}_8/\text{Li}_2\text{S}_n$  and the surface of  $\text{M}_2\text{CT}_2$ , the CDD between  $\text{M}_2\text{CT}_2$  monolayer and  $\text{S}_8/\text{Li}_2\text{S}_n$  are calculated as shown in Fig. 6 with the calculation details located in ESI<sup>†</sup>. The  $\text{S}_8$  and  $\text{M}_2\text{CF}_2$

interface exhibits negligible charge transfer, signifying the absence of chemical bond formation between the adsorbed sulfur species and the substrate. In contrast,  $\text{S}_8/\text{Li}_2\text{S}_n$  adsorption on  $\text{M}_2\text{CO}_2$  exhibits significantly enhanced interfacial electron redistribution. Lithiation induces pronounced electron accumulation at  $\text{Li}_2\text{S}_n/\text{M}_2\text{CT}_2$  interfaces, accompanied by intensified charge transfer indicative of Li–T (T = F/O) covalent bond formation. Concurrently, expanding electron-deficient domains within  $\text{Li}_2\text{S}_n$  reflect destabilization of Li–S and S–S bonding interactions. It can be deduced that chemical bonds are established between  $\text{Li}_2\text{S}_n$  and  $\text{M}_2\text{CT}_2$  during the lithiation process, which agrees with the trend of the adsorption energy. Moreover, the decomposition pathways of LiPSs are critically governed by two concurrent mechanisms: interfacial stabilization through Li–T (T = F/O) covalent bond formation and structural destabilization *via* progressive cleavage of Li–S and S–S bonds within  $\text{Li}_2\text{S}_n$  species.

The electronic structures of the substrate undergo changes following LiPSs adsorption, which is investigated by analyzing

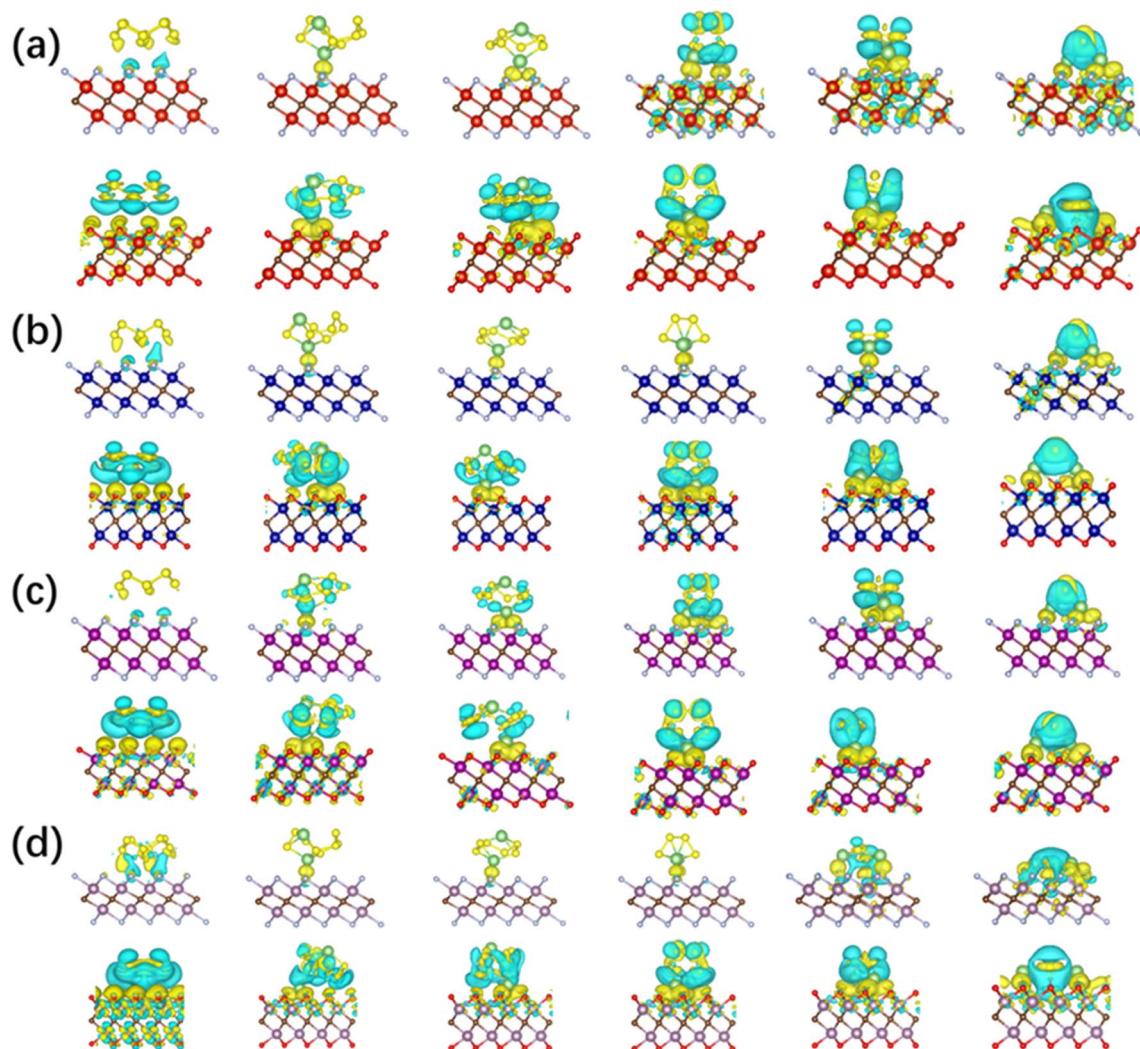


Fig. 6 Side views of CDD maps of  $\text{S}_8$  and  $\text{Li}_2\text{S}_n$  on (a)  $\text{V}_2\text{CT}_2$ , (b)  $\text{Cr}_2\text{CT}_2$ , (c)  $\text{Mn}_2\text{CT}_2$ , and (d)  $\text{Mo}_2\text{CT}_2$  monolayer (isosurface =  $\pm 0.002$  au for  $\text{Li}_2\text{S}_n$ , and isosurface =  $\pm 0.0002$  au for  $\text{S}_8$ ). The yellow and blue region indicate electron accumulation and depletion, respectively.



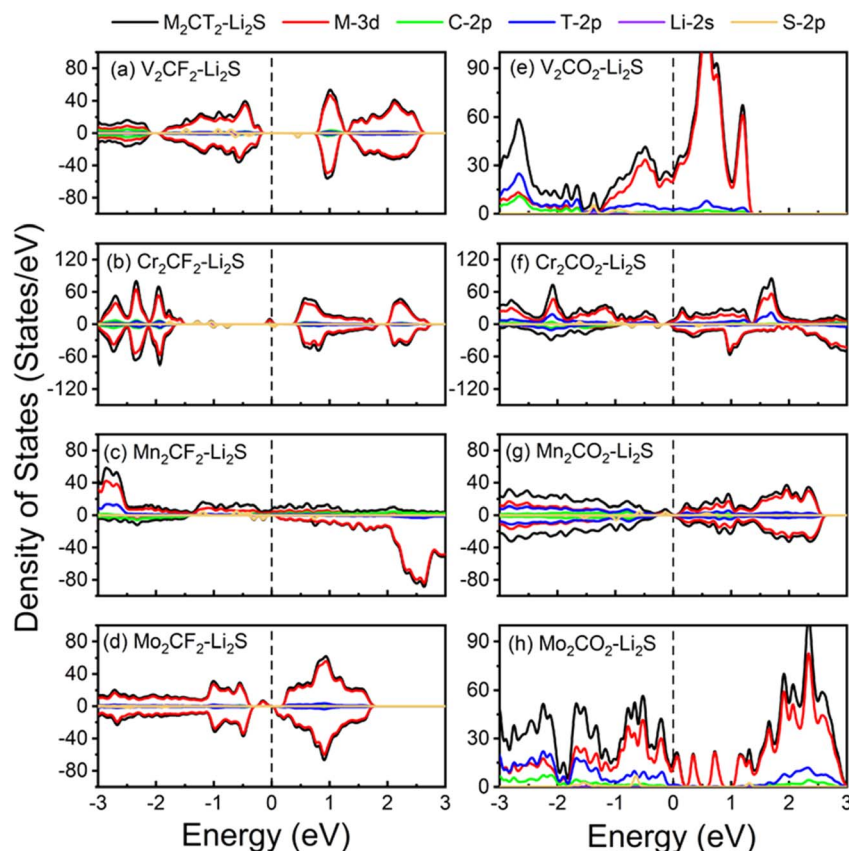


Fig. 7 Projected density of states of (a–h)  $M_2CT_2$  monolayer after the adsorption of  $Li_2S$ , respectively. The Fermi level is set at zero.

the PDOS of  $M_2CT_2$  after  $Li_2S$  adsorption. The PDOS of  $M_2CT_2$  monolayer after the adsorption of  $Li_2S$  are shown in Fig. 7. Compared with the PDOS of  $M_2CT_2$  monolayer, the Fermi level of  $M_2CT_2-Li_2S$  has shifted upwards with the electronic state of S atoms appearing in the band gap for the  $Mo_2CF_2-$ ,  $Cr_2CF_2-$ ,  $Mn_2CO_2-$ ,  $Mo_2CO_2-$ , and  $Cr_2CO_2-Li_2S$  systems. Therefore, the band gap of  $V_2CF_2$  and  $Cr_2CF_2$  became narrow, while  $Mo_2CF_2$ ,  $Cr_2CO_2$ , and  $Mn_2CO_2$  exhibit metallic characters after the adsorption of  $Li_2S$ . Overall, the conductivity of  $M_2CT_2$  is enhanced with the adsorption of  $Li_2S$ , which is benefit for the electron transportation.

### Electrocatalysis of $M_2CT_2$ on discharge/charging kinetics

The chemisorption intensity of  $Li_2S_n$  species critically modulates electrochemical reaction kinetics. Overly robust binding interactions may restrict surface mobility of redox-active intermediates, consequently impairing charge transfer efficiency. Such kinetic constraints during sulfur redox cycling constitute a fundamental performance limitation in Li-S battery systems.<sup>54,55</sup> The SRR pathways on  $M_2CT_2$  surfaces are systematically mapped through density functional theory (DFT) calculations, with the thermodynamic Gibbs free energy change ( $\Delta G$ ) for each reaction intermediate from  $S_8$  to  $Li_2S$  quantitatively presented in Fig. 8 and Table S3.<sup>†</sup> The calculation route of the SRR refers to the previous reports.<sup>51,52</sup> Obviously, the steps from  $S_8$  to  $Li_2S_8$  are all spontaneous exothermic on all the

calculated  $M_2CT_2$ , which indicates that the  $S_8$  can be readily converted into  $Li_2S_8$ . All reduction steps from  $Li_2S_8$  to  $Li_2S$  are found to be endothermic, with the sole exception of the  $Li_2S_6 \rightarrow Li_2S_4$  step. The rate-limiting step is identified as  $Li_2S_4 \rightarrow Li_2S_2$  for  $V_2CO_2$ ,  $Mo_2CF_2$ , and  $Mo_2CO_2$ , whereas for  $V_2CF_2$ ,  $Cr_2CF_2$ ,  $Cr_2CO_2$ ,  $Mn_2CF_2$ , and  $Mn_2CO_2$ , the  $Li_2S_2 \rightarrow Li_2S$  step served as the kinetic bottleneck. The endergonic  $Li_2S_2 \rightarrow Li_2S$  transition stems from the inherent kinetic limitations of solid-state conversion processes, aligning with established theoretical

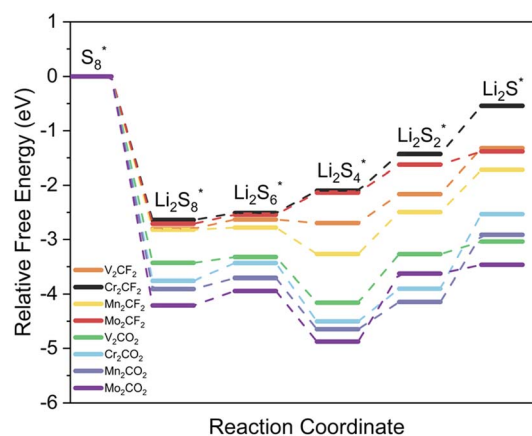


Fig. 8 The calculation of Gibbs free energy change ( $\Delta G$ ) of SRR on MXene monolayers.



frameworks in sulfur electrochemistry.<sup>56,57</sup> The Gibbs free energy change barrier ( $\Delta G_{\text{barrier}}$ ) for the rate-limiting step follow the sequence:  $\text{Mo}_2\text{CF}_2$  (0.51 eV) <  $\text{Mn}_2\text{CF}_2$  (0.78 eV) <  $\text{V}_2\text{CF}_2$  (0.84 eV) <  $\text{Cr}_2\text{CF}_2$  (0.88 eV) <  $\text{V}_2\text{CO}_2$  (0.89 eV) <  $\text{Mn}_2\text{CO}_2$  (1.23 eV) <  $\text{Mo}_2\text{CO}_2$  (1.25 eV) <  $\text{Cr}_2\text{CO}_2$  (1.37 eV). It is easy to find that the  $\text{M}_2\text{CF}_2$  have lower rate-limiting step reaction energy barrier than those of  $\text{M}_2\text{CO}_2$ , which proves that the F atom greatly enhances the catalytic activity of the SRR.

The elevated dissociation energy barrier of  $\text{Li}_2\text{S}$ , the terminal discharge product, significantly impedes electrochemical cycling reversibility.<sup>58,59</sup> This necessitates efficient delithiation kinetics ( $\text{Li}_2\text{S} \rightarrow \text{Li} + \text{Li}^+ + \text{e}^-$ ) to sustain charging efficiency. Fig. 9 quantitatively delineates the atomic-scale decomposition pathways of  $\text{Li}_2\text{S}$  on  $\text{M}_2\text{CT}_2$  monolayers, revealing the critical decomposition energy barriers. The minimum decomposition barriers of  $\text{Li}_2\text{S}$  are 0.27, 0.32, 0.51, and 0.53 eV on  $\text{Mo}_2\text{CO}_2$ ,  $\text{V}_2\text{CO}_2$ ,  $\text{Cr}_2\text{CO}_2$  and  $\text{Mn}_2\text{CO}_2$ , respectively, while they are 0.74, 0.80, 0.90, and 1.00 eV on  $\text{Mn}_2\text{CF}_2$ ,  $\text{Mo}_2\text{CF}_2$ ,  $\text{V}_2\text{CF}_2$  and  $\text{Cr}_2\text{CF}_2$ ,

respectively. Similar to the decomposition barrier of  $\text{Li}_2\text{S}$  on  $\text{Ti}_3\text{C}_2\text{F}_2$  (0.90 eV) and  $\text{Ti}_3\text{C}_2\text{O}_2$  (0.41 eV),<sup>60</sup> all the  $\text{M}_2\text{CT}_2$  greatly reduce the decomposition barriers, which indicate great catalytic effect for the decomposition reaction. Studies attribute this phenomenon to MXenes' metal-to-carbon (M/C) ratio, where elevated transition metal content (M) enhances  $\text{Li}_2\text{S}$  dissociation kinetics through optimized d-band electronic interactions.<sup>27</sup> The results indicate that the  $\text{M}_2\text{CT}_2$  could promote the decomposition of  $\text{Li}_2\text{S}$ , which enhances the electrochemical kinetics performance of Li-S batteries.

The charging mechanism initiates with the delithiation of the terminal discharge product  $\text{Li}_2\text{S}$ , where ion migration dynamics critically govern decomposition and nucleation processes. Of particular significance is the interfacial  $\text{Li}^+$  diffusion kinetics across the cathode substrate, prompting systematic analysis of  $\text{Li}^+$  migration energy barriers. Therefore, the activation energy barriers for  $\text{Li}^+$  diffusion across the cathode are quantified through NEB simulations. Three kinds of the

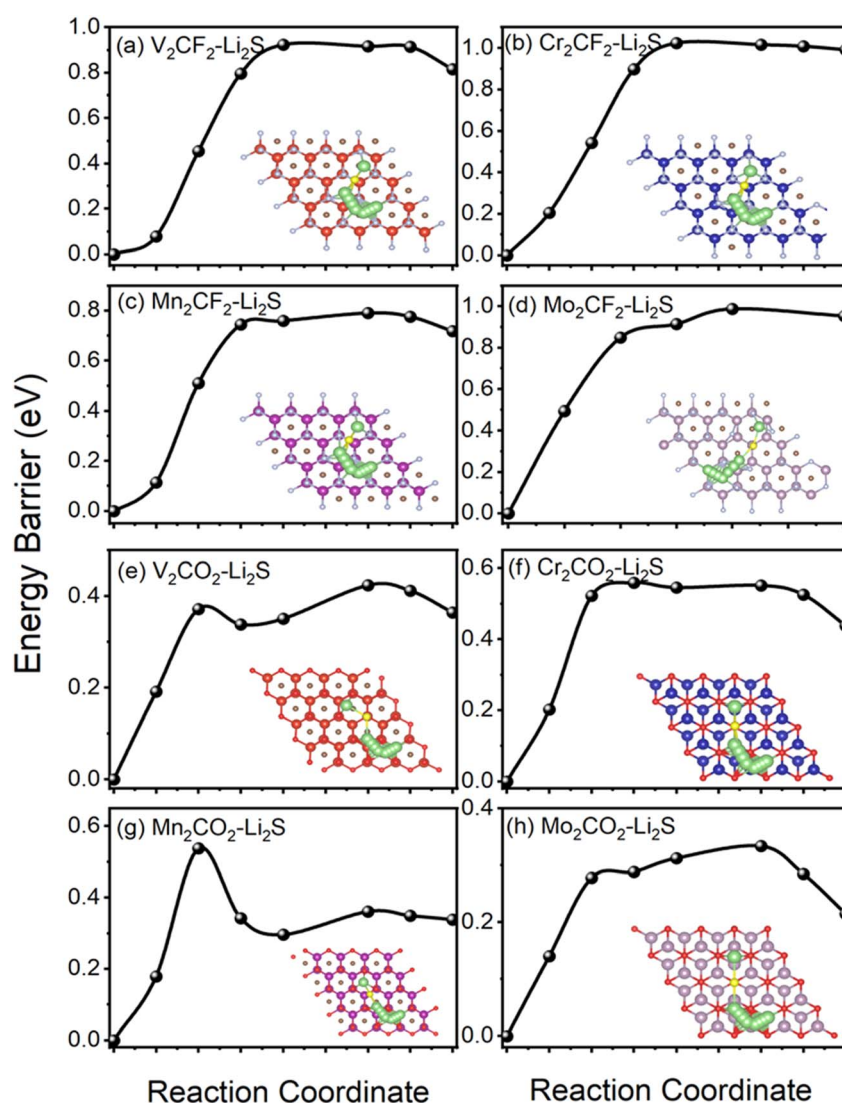


Fig. 9 Decomposition energies and decomposition paths of  $\text{Li}_2\text{S}$  on (a)  $\text{V}_2\text{CF}_2$ , (b)  $\text{Cr}_2\text{CF}_2$ , (c)  $\text{Mn}_2\text{CF}_2$ , (d)  $\text{Mo}_2\text{CF}_2$ , (e)  $\text{V}_2\text{CO}_2$ , (f)  $\text{Cr}_2\text{CO}_2$ , (g)  $\text{Mn}_2\text{CO}_2$ , and (h)  $\text{Mo}_2\text{CO}_2$  monolayer.



migration paths of  $\text{Li}^+$  are considered for Fcc and Hcp structure as presented in Fig. S5 (a) and (b),<sup>†</sup> respectively, and the diffusion barriers with different migration paths are shown in Fig. 10. It is found that the path 3 (the path 6) is the most difficult migration path for Fcc (Hcp) structure, while the diffusion barriers of the path 1 (the path 4) and the path 2 (the path 5) are comparable for all the calculated  $\text{M}_2\text{CT}_2$ . As shown in Fig. S5,<sup>†</sup> on  $\text{V}_2\text{CT}_2$ ,  $\text{Cr}_2\text{CF}_2$ ,  $\text{Mn}_2\text{CT}_2$  and  $\text{Mo}_2\text{CF}_2$ , the  $\text{Li}^+$  tend to move along the path 2 ( $\text{C1} \rightarrow \text{M} \rightarrow \text{C2}$ ), while on  $\text{Cr}_2\text{CO}_2$  and  $\text{Mo}_2\text{CO}_2$ , the  $\text{Li}^+$  prefers to be along the path 5 ( $\text{H1} \rightarrow \text{C} \rightarrow \text{H2}$ ). The smallest diffusion barriers of  $\text{Li}^+$  on the different  $\text{M}_2\text{CT}_2$  follow the sequence:  $\text{Mo}_2\text{CO}_2$  (0.11 eV) <  $\text{Cr}_2\text{CO}_2$  (0.12 eV) <  $\text{V}_2\text{CO}_2$  (0.13 eV) <  $\text{Mn}_2\text{CF}_2$  (0.16 eV) <  $\text{Mn}_2\text{CO}_2$  (0.25 eV) <  $\text{V}_2\text{CF}_2$  (0.32 eV) <  $\text{Cr}_2\text{CF}_2$  (0.33 eV) <  $\text{Mo}_2\text{CF}_2$  (0.44 eV). These relatively low diffusion barriers of  $\text{Li}^+$  promise the rapid diffusion of  $\text{Li}^+$  on the  $\text{M}_2\text{CT}_2$  surface and conversion of LiPSs during the charge process.

The decomposition of  $\text{Li}_2\text{S}$ , the diffusion of  $\text{Li}^+$ , and the catalytic activity of the SRR of the studied  $\text{M}_2\text{CT}_2$  are compared with that of the available F/O-functionalized MXenes as listed in Table S4.<sup>†</sup> (ref. 27 and 61) It is found that the decomposition barriers of  $\text{Li}_2\text{S}$  for  $\text{M}_2\text{CT}_2$  (0.27–1.00 eV) are apparently lower than those of  $\text{V}_2\text{NF}_2$  (2.31 eV),  $\text{V}_2\text{NO}_2$  (1.55 eV), and graphene (1.81 eV). Regarding the migration dynamics of  $\text{Li}^+$ , the diffusion barriers of  $\text{Li}^+$  on the  $\text{M}_2\text{CT}_2$  substrate (0.11 eV–0.44 eV) are close to those of  $\text{V}_2\text{NF}_2$  (0.17 eV),  $\text{V}_2\text{NO}_2$  (0.21 eV), and graphene (0.30 eV). Thus,  $\text{M}_2\text{CT}_2$  show great kinetic performance during the discharge/charging process with relatively small decomposition barriers of  $\text{Li}_2\text{S}$  and diffusion barriers of  $\text{Li}^+$ . What's more, the  $\Delta G_{\text{barrier}}$  of  $\text{M}_2\text{CT}_2$  (0.51 eV–1.37 eV) are significantly lower than those of  $\text{V}_2\text{NF}_2$  (2.14 eV) and  $\text{V}_2\text{NO}_2$  (1.88 eV), while they are comparable or lower than that of graphene (1.07 eV). Considering the above factors,  $\text{V}_2\text{CO}_2$  and  $\text{Mo}_2\text{CO}_2$  have the best electrocatalytic performance among the studied  $\text{M}_2\text{CT}_2$ , in

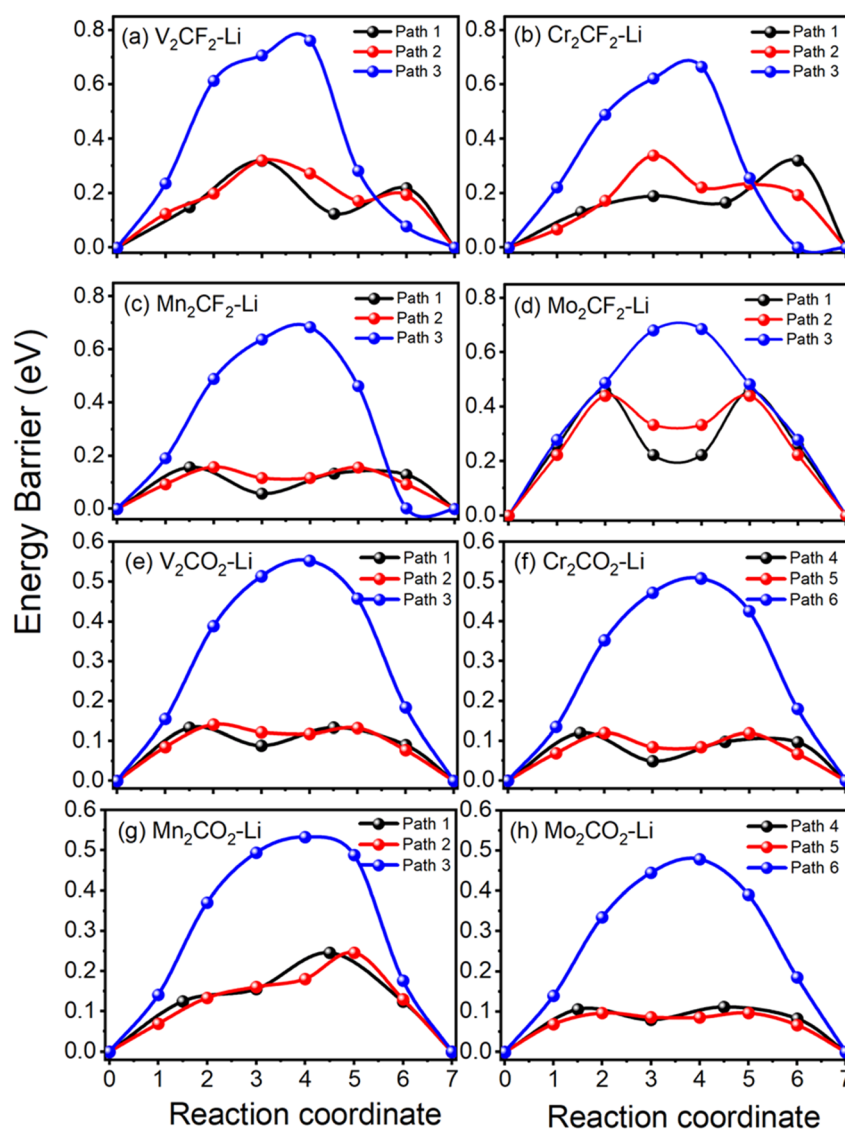


Fig. 10 Diffusion barriers with different migration paths of  $\text{Li}^+$  on (a)  $\text{V}_2\text{CF}_2$ , (b)  $\text{Cr}_2\text{CF}_2$ , (c)  $\text{Mn}_2\text{CF}_2$ , (d)  $\text{Mo}_2\text{CF}_2$ , (e)  $\text{V}_2\text{CO}_2$ , (f)  $\text{Cr}_2\text{CO}_2$ , (g)  $\text{Mn}_2\text{CO}_2$ , and (h)  $\text{Mo}_2\text{CO}_2$  monolayer.



which the decomposition barriers of  $\text{Li}_2\text{S}$  of  $\text{V}_2\text{CO}_2$  and  $\text{Mo}_2\text{CO}_2$  are only 0.32 eV and 0.27 eV, respectively, and the diffusion barriers of  $\text{Li}^+$  of  $\text{V}_2\text{CO}_2$  and  $\text{Mo}_2\text{CO}_2$  are 0.13 eV and 0.11 eV, respectively. Moreover, the  $\text{V}_2\text{CO}_2$  and  $\text{Mo}_2\text{CO}_2$  are metallic, which is beneficial for a fast charge/discharge rate. Therefore,  $\text{V}_2\text{CO}_2$  and  $\text{Mo}_2\text{CO}_2$  are the best choices for Li-S battery cathode material in the studied  $\text{M}_2\text{CT}_2$ .

The structural stability of electrode materials critically determines their cycling lifespan within operational voltage windows. To further investigate the stability as cathode materials for Li-S batteries, we calculate the energy of  $\text{Li}_2\text{S}$  adsorption on  $\text{V}_2\text{CO}_2$  and  $\text{Mo}_2\text{CO}_2$  through AIMD simulations at room temperature (300 K). As illustrated in Fig. S6,† the total energy fluctuations progressively diminish during simulation, while the structural frameworks remain intact throughout the process. Therefore, it is demonstrated that both  $\text{V}_2\text{CO}_2$  and  $\text{Mo}_2\text{CO}_2$  maintain excellent thermodynamic stability with  $\text{Li}_2\text{S}$  adsorption, and further validated their promise as highly prospective host materials for Li-S batteries.

## Conclusion

In summary, we systematically explore potential of  $\text{M}_2\text{CT}_2$  ( $\text{M} = \text{V}, \text{Cr}, \text{Mn}, \text{and Mo}$ ;  $\text{T} = \text{F and O}$ ) as anchoring materials and catalysts for Li-S batteries using DFT spin-polarized calculations. A moderate  $E_{\text{ads}}$  for  $\text{Li}_2\text{S}_n$  on  $\text{M}_2\text{CT}_2$  species are observed, which would restrain the shuttling of LiPSs and prevent capacity fading and enhance the cycling capability for Li-S batteries. The decomposition barriers of  $\text{Li}_2\text{S}$  (0.27 to 1.00 eV) and the  $\text{Li}^+$  diffusion barriers of  $\text{M}_2\text{CT}_2$  (0.11 to 0.44 eV) are relatively low, which would accelerate the formation and decomposition of solid  $\text{Li}_2\text{S}$  and hence redox reaction kinetics. It is also found that the  $\text{M}_2\text{CO}_2$  exhibit lower decomposition barriers of  $\text{Li}_2\text{S}$  and diffusion barriers of  $\text{Li}^+$  than  $\text{M}_2\text{CF}_2$ , especially for  $\text{V}_2\text{CO}_2$  and  $\text{Mo}_2\text{CO}_2$ . Moreover, the structures of  $\text{Li}_2\text{S}$  adsorbed  $\text{V}_2\text{CO}_2$  and  $\text{Mo}_2\text{CO}_2$  exhibit good thermodynamic stability at room temperature. All studied  $\text{M}_2\text{CT}_2$  exhibit relatively low  $\Delta G_{\text{barrier}}$  during the reaction process (0.51 to 1.37 eV), which would promote the conversion of LiPSs. Generally, the studied oxygen-terminated MXenes exhibit superior electrochemical performance compared to their fluorine-terminated MXenes.  $\text{V}_2\text{CO}_2$  and  $\text{Mo}_2\text{CO}_2$  are identified as the most promising candidates for Li-S battery host materials in the explored  $\text{M}_2\text{CT}_2$ . Our study not only provides critical insights for advancing  $\text{M}_2\text{CT}_2$  implementation in Li-S battery cathodes, but also expands further theoretical investigations into MXene-based materials.

## Data availability

The data that supports the findings of this study are available from the corresponding author upon reasonable request.

## Conflicts of interest

There are no conflicts to declare.

## Acknowledgements

This work is supported by the National Natural Science Foundation of China (No. 11904409 and 51572296), Youth Innovation Technology Project of Higher School in Shandong Province (2022KJ139), Postdoctoral Research Foundation of China (No. 2018M642721), and Shandong Postdoctoral Funded Project (201901012).

## References

- 1 B. Ding, J. Wang, Z. Fan, S. Chen, Q. Lin, X. Lu, H. Dou, A. Kumar Nanjundan, G. Yushin, X. Zhang and Y. Yamauchi, *Mater. Today*, 2020, **40**, 114–131.
- 2 W. Jin, X. Zhang, M. Liu, Y. Zhao and P. Zhang, *Energy Storage Mater.*, 2024, **67**, 103223.
- 3 R. Kumar, J. Liu, J.-Y. Hwang and Y.-K. Sun, *J. Mater. Chem. A*, 2018, **6**, 11582–11605.
- 4 A. D. Pathak, E. Cha and W. Choi, *Energy Storage Mater.*, 2024, **72**, 103711.
- 5 S. C. Kim, X. Gao, S. L. Liao, H. Su, Y. Chen, W. Zhang, L. C. Greenburg, J. A. Pan, X. Zheng, Y. Ye, M. S. Kim, P. Sayavong, A. Brest, J. Qin, Z. Bao and Y. Cui, *Nat. Commun.*, 2024, **15**, 1268.
- 6 Z. Lv, P. Wang, J. Wang, S. Tian and T. Yi, *J. Ind. Eng. Chem.*, 2023, **124**, 68–88.
- 7 J. Li, Y. Qu, C. Chen, X. Zhang and M. Shao, *Nanoscale*, 2021, **13**, 15–35.
- 8 J. T. Kim, A. Rao, H. Y. Nie, Y. Hu, W. Li, F. Zhao, S. Deng, X. Hao, J. Fu, J. Luo, H. Duan, C. Wang, C. V. Singh and X. Sun, *Nat. Commun.*, 2023, **14**, 6404.
- 9 Y. Chen, T. Wang, H. Tian, D. Su, Q. Zhang and G. Wang, *Adv. Mater.*, 2021, **33**, 2003666.
- 10 R. B. Nuwayhid, J. Yeom, H. O. Ford, Z. G. Neale, M. W. Swift, N. Bernstein, R. Carter and J. W. Long, *RSC Appl. Interfaces*, 2025, **2**, 472–483.
- 11 Z. Wu, M. Liu, W. He, T. Guo, W. Tong, E. Kan, X. Ouyang, F. Qiao, J. Wang, X. Sun, X. Wang, J. Zhu, A. Coskun and Y. Fu, *Nat. Commun.*, 2024, **15**, 9535.
- 12 J. Chai, J. Du, Q. Li, N. Han, W. Zhang and B. Tang, *Energy Fuel.*, 2021, **35**, 15455–15471.
- 13 S. Li, D. Leng, W. Li, L. Qie, Z. Dong, Z. Cheng and Z. Fan, *Energy Storage Mater.*, 2020, **27**, 279–296.
- 14 Y. Pan, Y. Zhu, Y. Li, H. Liu, Y. Cong, Q. Li and M. Wu, *Appl. Surf. Sci.*, 2023, **610**, 155507.
- 15 M. Naguib, M. Kurtoglu, V. Presser, J. Lu, J. Niu, M. Heon, L. Hultman, Y. Gogotsi and M. W. Barsoum, *Adv. Mater.*, 2011, **23**, 4248–4253.
- 16 W. Meng, X. Liu, H. Song, Y. Xie, X. Shi, M. Dargusch, Z.-G. Chen, Z. Tang and S. Lu, *Nano Today*, 2021, **40**, 101273.
- 17 X. Liang, A. Garsuch and L. F. Nazar, *Angew. Chem., Int. Ed.*, 2015, **54**, 3907–3911.
- 18 X. Zhao, M. Liu, Y. Chen, B. Hou, N. Zhang, B. Chen, N. Yang, K. Chen, J. Li and L. An, *J. Mater. Chem. A*, 2015, **3**, 7870–7876.
- 19 W. Cui, Z.-Y. Hu, R. R. Unocic, G. Van Tendeloo and X. Sang, *Chin. Chem. Lett.*, 2021, **32**, 339–344.



- 20 Q. Yang, S. J. Eder, A. Martini and P. G. Grützmacher, *npj Mater. Degrad.*, 2023, **7**, 6.
- 21 D. Rao, L. Zhang, Y. Wang, Z. Meng, X. Qian, J. Liu, X. Shen, G. Qiao and R. Lu, *J. Phys. Chem. C*, 2017, **121**, 11047–11054.
- 22 J. Hu, B. Xu, C. Ouyang, S. A. Yang and Y. Yao, *J. Phys. Chem. C*, 2014, **118**, 24274–24281.
- 23 X. Liu, X. Shao, F. Li and M. Zhao, *Appl. Surf. Sci.*, 2018, **455**, 522–526.
- 24 H. Lin, D.-D. Yang, N. Lou, S.-G. Zhu and H.-Z. Li, *Ceram. Int.*, 2019, **45**, 1588–1594.
- 25 C. Shi, X. Zhang, Z. Li, T. T. Beyene, T. Zheng, Y. Liu and K. Zhu, *Energy Fuels*, 2024, **38**, 14866–14890.
- 26 Q. Zhang, X. Zhang, Y. Xiao, C. Li, H. H. Tan, J. Liu and Y. Wu, *ACS Omega*, 2020, **5**, 29272–29283.
- 27 D. Wang, F. Li, R. Lian, J. Xu, D. Kan, Y. Liu, G. Chen, Y. Gogotsi and Y. Wei, *ACS Nano*, 2019, **13**, 11078–11086.
- 28 C. Lamiel, I. Hussain, J. H. Warner and K. Zhang, *Mater. Today*, 2023, **63**, 313–338.
- 29 L. Zhang, J. Shi, K. Niu, P. Jia, Y. Gao and G. Gao, *ACS Appl. Nano Mater.*, 2023, **6**, 20812–20822.
- 30 G. F. I. Kresse, *Phys. Rev. B:Condens. Matter Mater. Phys.*, 1996, **54**, 11169–11186.
- 31 J. P. B. Perdew and K. Burke, *Phys. Rev. Lett.*, 1996, **77**, 3865–3868.
- 32 G. F. I. Kresse, *Comput. Mater. Sci.*, 1996, **6**, 15–50.
- 33 V. I. Anisimov and a. O. K. A. Jan Zaanen, *Phys. Rev. B:Condens. Matter Mater. Phys.*, 1991, **44**, 943–954.
- 34 S. Bae, Y. G. Kang, M. Khazaei, K. Ohno, Y. H. Kim, M. J. Han, K. J. Chang and H. Raebiger, *Mater. Today Adv.*, 2021, **9**, 100118.
- 35 Q. Sun, Z. Fu and Z. Yang, *J. Magn. Magn. Mater.*, 2020, **514**, 167141.
- 36 X. Zhang, W. Meng, T. He, L. Jin, X. Dai and G. Liu, *Appl. Surf. Sci.*, 2020, **503**, 144091.
- 37 S. Grimme, J. Antony, S. Ehrlich and H. Krieg, *J. Chem. Phys.*, 2010, **132**, 154104.
- 38 G. U. Henkelman, B. P. Uberuaga and H. Jónsson, *J. Chem. Phys.*, 1991, **113**, 9901–9904.
- 39 M. Khazaei, M. Arai, T. Sasaki, C. Y. Chung, N. S. Venkataramanan, M. Estili, Y. Sakka and Y. Kawazoe, *Adv. Funct. Mater.*, 2012, **23**, 2185–2192.
- 40 P. Gao, M. Song, X. Wang, Q. Liu, S. He, Y. Su and P. Qian, *Nanomaterials*, 2022, **12**, 556.
- 41 J. He, P. Lyu and P. Nachtigall, *J. Mater. Chem. C*, 2016, **4**, 11143–11149.
- 42 Q. Sun, Z. Fu, Y. Li and Z. Yang, *J. Alloys Compd.*, 2021, **850**, 156769.
- 43 Z. Tan, Z. Fang, B. Li and Y. Yang, *ACS Omega*, 2020, **5**, 25848–25853.
- 44 L. Zhang, Y. Liu, M. Wu and G. Gao, *Adv. Funct. Mater.*, 2024, 2417857.
- 45 L. Zhang, Y. Liu, Z. Xu and G. Gao, *2D Mater.*, 2023, **10**, 045005.
- 46 C. Zhang, W. Chu, X. Hong, Q. He, R. Lu, X. Liao and Y. Zhao, *Chem. Eng. J.*, 2022, **439**, 135679.
- 47 G. Xu, X. Song, M. Jiang, R. Wang, S. Lian and X. Yang, *Appl. Catal., B*, 2025, **362**, 124707.
- 48 Z. Chen, S. Huang, X. Yuan, X. Gan and N. Zhou, *Appl. Surf. Sci.*, 2021, **544**, 148861.
- 49 Z. Chen, S. Huang, B. Huang, M. Wan and N. Zhou, *Appl. Surf. Sci.*, 2020, **509**, 145319.
- 50 Z. Chen, Z. Chang, Z. Liu and N. Zhou, *Appl. Surf. Sci.*, 2022, **602**, 154375.
- 51 X. Zhu, M. Ge, T. Sun, X. Yuan and Y. Li, *J. Phys. Chem. Lett.*, 2023, **14**, 2215–2221.
- 52 C. Wei, T. Fang, X. Tang, P. Wang and X. Liu, *J. Phys. Chem. C*, 2022, **126**, 17066–17075.
- 53 M. Cheviri and S. Lakshmipathi, *Comput. Theor. Chem.*, 2021, **1202**, 113323.
- 54 Z. Du, X. Chen, W. Hu, C. Chuang, S. Xie, A. Hu, W. Yan, X. Kong, X. Wu, H. Ji and L. J. Wan, *J. Am. Chem. Soc.*, 2019, **141**, 3977–3985.
- 55 G. Zhou, S. Zhao, T. Wang, S. Z. Yang, B. Johannessen, H. Chen, C. Liu, Y. Ye, Y. Wu, Y. Peng, C. Liu, S. P. Jiang, Q. Zhang and Y. Cui, *Nano Lett.*, 2020, **20**, 1252–1261.
- 56 Z. Yi, F. Su, L. Dai, Z. Wang, L. Xie, Z. Zuo, X. Chen, Y. Liu and C.-m. Chen, *Energy Storage Mater.*, 2022, **47**, 327–335.
- 57 Z. Jin, T. Lin, H. Jia, B. Liu, Q. Zhang, L. Li, L. Zhang, Z. M. Su and C. Wang, *ACS Nano*, 2021, **15**, 7318–7327.
- 58 Y. Fu, H. Wang, D. Li, J. Shen, Y. Liu, M. Wei and Q. Hu, *J. Alloys Compd.*, 2023, **965**, 171306.
- 59 X. T. Fang, L. Zhou, C. Chen, D. L. Danilov, F. Qiao, H. Li and P. H. L. Notten, *Molecules*, 2023, **28**, 7304.
- 60 H. Hong, N. A. R. Che Mohamad, K. Chae, F. Marques Mota and D. H. Kim, *J. Mater. Chem. A*, 2021, **9**, 10012–10038.
- 61 K. Fan, Y. Ying, X. Luo and H. Huang, *J. Mater. Chem. A*, 2021, **9**, 25391–25398.

